CrossMark

J/M PAPERS

# Unsteady effects in a hypersonic compression ramp flow with laminar separation

Shibin Cao[1],†, Jiaao Hao[2], Igor Klioutchnikov[1], Herbert Olivier[1] and Chih-Yung Wen[2,3]

[1]Shock Wave Laboratory, RWTH Aachen University, 52056 Aachen, Germany

[2]Department of Mechanical Engineering, The Hong Kong Polytechnic University, Kowloon, Hong Kong

[3]Interdisciplinary Division of Aeronautical and Aviation Engineering, The Hong Kong Polytechnic University, Kowloon, Hong Kong

Direct numerical simulations (DNS) are performed to investigate a hypersonic flow over a compression ramp with a free stream Mach number of 7.7 and a free stream Reynolds number of $4.2 \times 10^5$ based on the flat plate length. The DNS results are validated by comparison with experimental data and theoretical predictions. It is shown that even in the absence of external disturbances, streamwise heat flux streaks form on the ramp surface downstream of reattachment, and that they are non-uniformly distributed in the spanwise direction. The surface heat flux exhibits a low-frequency unsteadiness, which propagates in the streamwise direction. Additionally, the unsteadiness of the heat flux streaks downstream of reattachment is coupled with a pulsation of the reattachment position. By conducting a dynamic mode decomposition (DMD) analysis, several oscillatory modes, characterised by streamwise low-frequency periodicity, are revealed in the separation bubble flow. The DNS results are further explained by a global stability analysis (GSA). Particularly, the flow structure of the leading DMD modes is consistent with that of the oscillatory unstable modes identified by the GSA. It is therefore concluded that the global instabilities are responsible for the unsteadiness of the considered compression ramp flow.

**Key words:** boundary layer separation, shock waves

## 1. Introduction

Hypersonic flow over a compression ramp is a canonical case of shock-wave/boundary-layer interaction (SWBLI) and has been of great interest for more than half a century. Fundamental investigations of compression ramp flow contribute to the understanding of

† Email address for correspondence: cabinhit@outlook.com

the flow around control surfaces, engine inlets, body flaps, junctions, etc., of hypersonic vehicles. Under certain conditions, the ramp-induced pressure rise leads the boundary layer to separate ahead of the corner, forming a separation bubble and a complex shock system. Although the geometry of a compression ramp is two-dimensional, experiments (de Luca *et al.* 1995; Simeonides & Haase 1995; Chuvakhov *et al.* 2017; Roghelia *et al.* 2017*a*,*b*) and numerical simulations (Ohmichi & Suzuki 2013; Cao, Klioutchnikov & Olivier 2019*a*) showed the presence of streamwise streaks in the vicinity of flow reattachment. The streamwise streaks manifest themselves in variations of surface heat flux, wall pressure, skin friction, etc., and they can usually persist for a certain distance post-reattachment until transition to turbulence occurs (Simeonides & Haase 1995; Roghelia *et al.* 2017*b*).

The presence of streamwise streaks or associated streamwise vortices was also found for other configurations such as a hollow cylinder flare (Benay *et al.* 2006), a double wedge (Yang *et al.* 2012), oblique SWBLI (Hildebrand *et al.* 2018) and scramjet forebody (Matsumura, Schneider & Berry 2005). Many studies have focused on the physical mechanism responsible for the formation of the streamwise streaks. Early studies proposed leading edge imperfections as a source of disturbances which are amplified downstream, forming the streamwise vortices. However, Matsumura *et al.* (2005) and Roghelia *et al.* (2017*b*) demonstrated the presence of heat flux streaks on the compression ramps with a well-prepared sharp leading edge. Additionally, Roghelia *et al.* (2017*a*) reported an almost identical wavelength on the compression ramps at two facilities for similar flow conditions and model configuration. This suggests that external disturbances (for example, induced by leading edge imperfections, free stream turbulence and surface roughness) can be an excitation but cannot explain the matching streaks observed in different facilities.

On the other hand, the experimentally or numerically observed heat flux striation phenomenon has been often attributed to the formation of Görtler-like vortices supported by the concave flow curvature in the reattaching flow regions (de Luca *et al.* 1995; Simeonides & Haase 1995; Navarro-Martinez & Tutty 2005; Roghelia *et al.* 2017*a*,*b*; Cao *et al.* 2019*a*). The estimated favourable Görtler number near reattachment provides evidence for the significance of centrifugal instability. Recently, utilising an input–output analysis, Dwivedi *et al.* (2019) were able to analyse the formation of streamwise streaks as a result of the amplification of external disturbances in a compression ramp flow. It was shown that baroclinic effects arising from the interactions of base-flow density gradients with spanwise gradients of pressure perturbations play a dominant role in triggering the streamwise streaks. Therefore, baroclinic effects and centrifugal effects are two potential mechanisms that can amplify upstream disturbances, leading to vortical structures (Zapryagaev, Kavun & Lipatov 2013).

In addition to these two effects, more attention is turned to instabilities in the separation bubble flow and their connection to the streamwise streaks. It is known that beyond a critical condition (for instance a critical turn angle of the ramp), a two-dimensional flow bifurcates to a three-dimensional one due to global instabilities (Theofilis, Hein & Dallmann 2000; Robinet 2007; Hildebrand *et al.* 2018; Sidharth *et al.* 2018). By performing global linear stability analysis for a double wedge flow, Sidharth *et al.* (2018) showed that in the absence of external disturbances, the three-dimensionality in the separation bubble results in temperature streaks on an adiabatic wall, and the instabilities are intrinsic to the separation bubble flow. A significant contribution of the separation bubble flow to the wavelength selection mechanism of the streamwise streaks was also demonstrated by Dwivedi *et al.* (2019). Furthermore, for a steady-state base flow at a higher turn angle, Sidharth *et al.* (2018) found a family of globally unstable modes including an

oscillatory one. This mode exhibits streamwise periodicity in the separation bubble. Several unsteady modes were also revealed for a compression ramp flow over a heated wall (Sidharth *et al.* 2017). These results indicate that for a base flow far beyond the bifurcation point, unsteady effects are present.

The experimentally observed streamwise streaks usually exhibit a time-averaged behaviour due to the utilised measurement techniques such as oil flow visualisation, infrared imaging and temperature sensitive paint (Simeonides & Haase 1995; Yang *et al.* 2012; Roghelia *et al.* 2017a). As a result, investigation of the unsteadiness of streamwise streaks is scarce. Zapryagaev *et al.* (2013) and Kavun, Lipatov & Zapryagaev (2019) analysed the wall pressure fluctuations in the reattachment region for a compression ramp flow at a free stream Mach number of 6 and revealed two local maxima in the spectra of pressure fluctuations. The lower one had a Strouhal number of 0.64 and was interpreted by the longitudinal pulsation of the reattachment position (Kavun *et al.* 2019). Cao *et al.* (2019a), Cao, Klioutchnikov & Olivier (2019b) performed direct numerical simulations (DNS) to investigate compression ramp flows at a free stream Mach number of 7.7. Unsteady flow features were uncovered both for the separation bubble flow and for the surface heat fluxes downstream of reattachment. However, the relation between the instability of separation bubble flow and the downstream unsteady streaks is still not clear.

Direct numerical simulation is an ideal tool to investigate the intrinsic instability and unsteadiness in a compression ramp flow because it has the advantage of creating a nearly disturbance-free environment. By using DNS, one can study a naturally generated three-dimensional flow field without adding external noise. Additionally, global stability analysis (GSA) has been proven to be useful in understanding the instability mechanisms of laminar separation bubbles (Robinet 2007; Theofilis 2011; Sidharth *et al.* 2017, 2018; Hildebrand *et al.* 2018). It considers the linear stability of small-amplitude perturbations superposed on a steady base flow without assumptions on the spatial variation of the base flow and the directionality of perturbation waves (Sidharth *et al.* 2018). This makes GSA suitable for studying the stability of flows with separation. In view of this, we focus on the laminar separated compression ramp flow which is globally unstable. Particularly, we employ DNS and GSA to investigate the flow unsteadiness triggered by the global instability.

In this paper, we consider the compression ramp flow experimentally investigated by Roghelia *et al.* (2017b). By performing GSA, we show that global unstable modes, both stationary and oscillatory, exist in the separation bubble flow, which is verified by DNS. The contribution of global instability to the formation of streamwise streaks is confirmed. The flow unsteadiness is shown to have its origin in the separation bubble flow. The present paper extends the studies on the intrinsic instability of a fluid dynamic system (Sidharth *et al.* 2017, 2018; Hildebrand *et al.* 2018) and provides more physical insights into the unsteadiness in a laminar separated flow.

The paper is organised as follows. Details about the numerical methodology, the flow conditions and the compression ramp geometry are given in § 2, where the validation of the DNS solver and grid convergence are also discussed. Section 3 provides a detailed description of the flow establishment and an extensive comparison between the DNS results and the GSA predictions. In § 4, the unsteady features are shown separately for the surface heat flux post-reattachment and the flow near reattachment. The unsteady flow structures in the separation bubble flow are analysed in § 5 by employing dynamic mode decomposition (DMD). Concluding remarks are provided in § 6.

## 2. Numerical methodology

### 2.1. *DNS*

Direct numerical simulations with a robust shock capturing feature are applied to study the hypersonic compression ramp flow problem. The three-dimensional Navier–Stokes equations for unsteady, compressible flow are considered in curvilinear coordinates in conservative non-dimensional form,

$$\frac{\partial U}{\partial t} + \frac{\partial F}{\partial \xi} + \frac{\partial G}{\partial \eta} + \frac{\partial H}{\partial \zeta} = \frac{\partial F^\nu}{\partial \xi} + \frac{\partial G^\nu}{\partial \eta} + \frac{\partial H^\nu}{\partial \zeta}. \tag{2.1}$$

Here, $U$ is the solution vector, $F$, $G$ and $H$ are the inviscid fluxes, and $F^\nu$, $G^\nu$ and $H^\nu$ denote the viscous fluxes. Here $U$, $F$ and $F^\nu$ are defined as

$$U = J \begin{pmatrix} \rho^* \\ \rho^* u^* \\ \rho^* v^* \\ \rho^* w^* \\ \rho^* e^* \end{pmatrix}, \quad F = J \begin{pmatrix} \rho^* \theta^* \\ \rho^* \theta^* u^* + \xi_x p^* \Upsilon \\ \rho^* \theta^* v^* + \xi_y p^* \Upsilon \\ \rho^* \theta^* w^* + \xi_z p^* \Upsilon \\ \rho^* \theta^* \left( e^* + \dfrac{p^*}{\rho^*} \Upsilon \right) \end{pmatrix}, \quad F^\nu = J \begin{pmatrix} 0 \\ \Psi(\xi_x \tau^*_{\xi\xi} + \xi_y \tau^*_{\xi\eta} + \xi_z \tau^*_{\xi\zeta}) \\ \Psi(\xi_x \tau^*_{\eta\xi} + \xi_y \tau^*_{\eta\eta} + \xi_z \tau^*_{\eta\zeta}) \\ \Psi(\xi_x \tau^*_{\zeta\xi} + \xi_y \tau^*_{\zeta\eta} + \xi_z \tau^*_{\zeta\zeta}) \\ \Psi(u^*(\xi_x \tau^*_{\xi\xi} + \xi_y \tau^*_{\xi\eta} + \xi_z \tau^*_{\xi\zeta}) \\ +v^*(\xi_x \tau^*_{\eta\xi} + \xi_y \tau^*_{\eta\eta} + \xi_z \tau^*_{\eta\zeta}) \\ +w^*(\xi_x \tau^*_{\zeta\xi} + \xi_y \tau^*_{\zeta\eta} + \xi_z \tau^*_{\zeta\zeta})) \\ -\Gamma(\xi_x q^*_\xi + \xi_y q^*_\eta + \xi_z q^*_\zeta) \end{pmatrix}, \tag{2.2a-c}$$

where

$$\theta^* = u^* \xi_x + v^* \xi_y + w^* \xi_z, \quad \Upsilon = \frac{1}{\gamma M^2_\infty}, \quad \Psi = \frac{1}{Re_{\infty,L}}, \quad \Gamma = \frac{1}{(\gamma-1)M^2_\infty Pr}, \tag{2.3a-d}$$

and $\xi_{x,y,z}$ are the metric coefficients and $J$ the determinant of the Jacobian matrix of the transformation of the Cartesian coordinates $x$, $y$ and $z$ into the curvilinear coordinates $\xi(x, y, z)$, $\eta(x, y, z)$ and $\zeta(x, y, z)$. Here $\tau^*$ and $q^*$ are the transformed shear stress tensor and heat flux vector, respectively. The total energy $e^*$ is defined as

$$e^* = \frac{u^{*2} + v^{*2} + w^{*2}}{2} + \frac{\Upsilon}{\gamma-1}\frac{p^*}{\rho^*}. \tag{2.4}$$

Note that other flux terms are not shown due to their similar form (Gageik, Klioutchnikov & Olivier 2015). The system of equations is closed by the perfect gas law relating the density $\rho$, the pressure $p$ and the temperature $T$. Sutherland's law is used to determine the viscosity $\mu$. The ratio of specific heats $\gamma$ and the Prandtl number $Pr$ used in the simulations are 1.4 and 0.71, respectively. The non-dimensional variables are normalised using the free stream parameters: $\rho^* = \rho/\rho_\infty$, $u^* = u/u_\infty$, $p^* = p/p_\infty$, $e^* = e/u^2_\infty$ and $T^* = T/T_\infty$. The flat plate length $L$ is used as the reference length.

In terms of the numerical methods, time integration is performed by an explicit third-order total variation diminishing (known as TVD) Runge–Kutta scheme. A weighted essentially non-oscillatory (known as WENO) finite difference scheme of fifth order is applied for the discretisation of the inviscid fluxes, based on the work of

| $M_\infty$ | $Re_\infty$ | $h_0$ | $T_\infty$ | $p_\infty$ | $u_\infty$ | $T_w$ |
|---|---|---|---|---|---|---|
| — | (m$^{-1}$) | (MJ kg$^{-1}$) | (K) | (Pa) | (m s$^{-1}$) | (K) |
| 7.7 | $4.2 \times 10^6$ | 1.7 | 125 | 760 | 1726 | 293 |

Table 1. Flow conditions at the shock tunnel TH2 (Roghelia *et al.* 2017*b*).

Jiang & Shu (1996). A sixth-order central difference scheme is used to approximate the viscous fluxes. Details about the numerical schemes may be found in Hermes, Klioutchnikov & Olivier (2012) and Gageik *et al.* (2015). The DNS solver has been validated and successfully applied for many cases and especially in studying hypersonic compression ramp flows (Klioutchnikov, Cao & Olivier 2017; Cao *et al.* 2019*a*,*b*; Cao, Klioutchnikov & Olivier 2020).

### 2.2. *Compression ramp configuration, flow condition and mesh resolution*

The numerically considered flow conditions and compression ramp geometry are mainly based on those used in the experimental campaign carried out in the hypersonic Aachen shock tunnel TH2 at the Shock Wave Laboratory of RWTH Aachen University (Roghelia *et al.* 2017*a*,*b*). The compression ramp comprises a flat plate with a sharp leading edge followed by a ramp with a deflection angle of 15°. The lengths of the flat plate and the ramp are both 100 mm. Table 1 lists the flow conditions at the shock tunnel TH2, which are adopted from Roghelia *et al.* (2017*b*). The free stream Mach number ($M_\infty$) and Reynolds number ($Re_{\infty,L}$) are 7.7 and $4.2 \times 10^5$, respectively. The total enthalpy $h_0$ is relatively low allowing the use of the perfect gas assumption. Due to the short running time of the shock tunnel (Roghelia *et al.* 2017*b*), an isothermal wall condition is applied, and the wall temperature ($T_w$) is given by 293 K.

Two mesh cases (G1 and G2) are considered for a grid-convergence study. The mesh resolution, i.e. the number of grid points in streamwise ($x$), wall-normal ($y$) and spanwise ($z$) directions, is $1080 \times 240 \times 480$ and $1600 \times 320 \times 240$ for cases G1 and G2, respectively. As shown in figure 1, the mesh is clustered near the leading edge (left) and the wall (bottom). The mesh spacing at the wall is $\Delta y = 8 \times 10^{-6}$ m for case G1 and $\Delta y = 5 \times 10^{-6}$ m for case G2, yielding a non-dimensional wall-distance at the position immediately upstream of separation of $y_{wall}^+ \approx 0.3$ and 0.2, respectively. It is noted that the upstream flat plate boundary layer is laminar with a thickness of 1.38 mm at the separation position. The number of grid points inside the boundary layer at the separation position is 75 for case G1 and 118 for case G2. In the spanwise direction, the mesh is uniformly distributed. The spanwise length of the physical domain for cases G1 and G2 is 100 mm and 30 mm, respectively, while in the experiments the model span was 200 mm. Therefore, the mesh resolution for case G2 is higher than for case G1 in all three directions. Preliminary two-dimensional simulations showed that the converged steady-state flow fields are almost identical for both cases. Results for the three-dimensional simulations are compared below.

### 2.3. *Boundary and initial conditions*

In terms of the conditions at the numerical inlet boundary, twenty grid points are placed up to 1 mm ahead of the leading edge to establish the free stream. The free stream condition is also prescribed at the upper computational boundary. An extrapolation condition is used at the outflow boundary. For the no-slip wall, isothermal conditions are specified with the
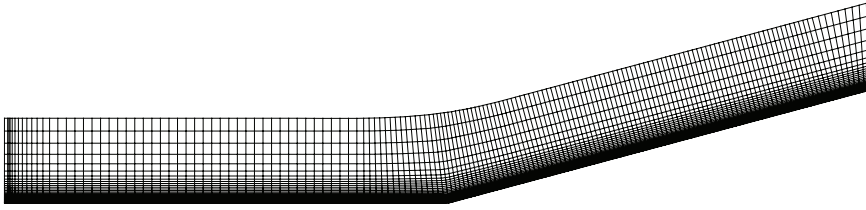
Figure 1. Mesh distribution in *x*–*y* plane for case G1 (each 10th point is shown).

wall temperature being 293 K. Periodic boundary conditions are applied in the spanwise direction.

To accelerate the computation, the three-dimensional simulations are initialised by duplicating the two-dimensional converged solution in the spanwise direction. Initial values of the spanwise velocity component ($w$) are only imposed at the first time step. In particular, random values ranging from $w/u_\infty = -0.01$ to $w/u_\infty = 0.01$ are introduced for the first twenty grid points normal to the wall at $0.5 < x/L < 1.5$. These initial disturbances dissipate quickly but speed up the formation of three-dimensionality. It has been demonstrated by Cao *et al.* (2019*b*) that when the spanwise velocity component was initially set to zero, three-dimensionality still occurred in the flow field due to the amplification of the low-level disturbances resulting from numerical round-off errors. Moreover, the wavelength of the heat flux streaks remained unaltered compared with the case with initial random values for $w$.

### 2.4. *Run time of simulations*

In the three-dimensional simulations, a fully developed flow field is established within 3.5 ms (or $tu_\infty/L = 60$), as shown in § 3.1. For maintaining consistency, the non-dimensional time scale ($tu_\infty/L$) is used in the following. It should be noted that $tu_\infty/L = 0$ corresponds to the beginning of the three-dimensional simulations. In order to study the unsteady effects in the flow field, we extend the simulation for case G1 up to $tu_\infty/L = 130$ to cover many cycles of the unsteadiness. A great number of instantaneous DNS data are collected so as to perform statistical analysis. The sampling time interval for collecting the data is $\Delta tu_\infty/L = 0.03$.

### 2.5. *Validation and grid independence*

Although the DNS solver has been validated previously (Cao *et al.* 2019*a*, 2020), it is worth comparing the numerical results with the experimental results of Roghelia *et al.* (2017*b*). Figure 2(*a*) shows the comparison for the surface pressure coefficient ($C_p$) and the wall Stanton number ($St$), which is defined as

$$St = \frac{q_w}{\rho_\infty u_\infty c_p (T_{aw} - T_w)}, \tag{2.5}$$

where $q_w$ is the surface heat flux, $c_p$ is specific heat capacity and $T_{aw}$ is the adiabatic wall temperature. The time-averaged data are taken along the line of symmetry of the model. In general, the DNS results (e.g. the separation bubble length, the magnitudes of pressure and heat flux) agree well with the experimental data. The discrepancy in the pressure upstream of separation may result from a limited lower resolution of the installed pressure transducers in the experiments, because in this region the pressure
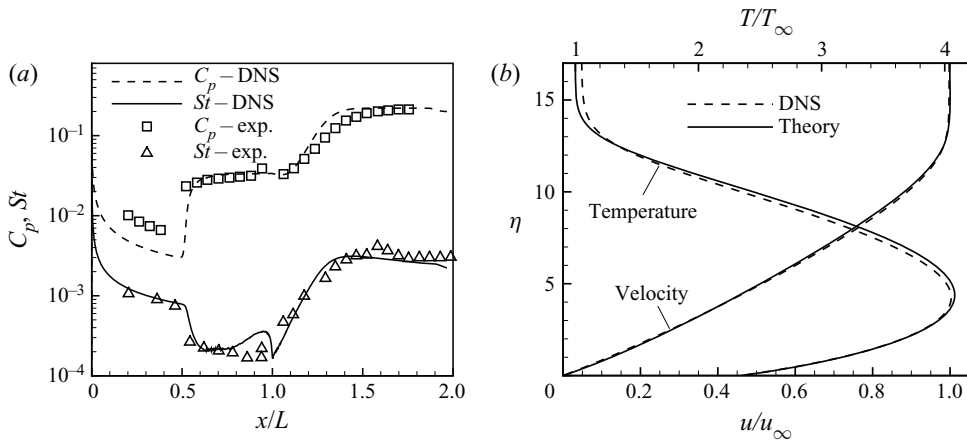
Figure 2. (*a*) Comparison of the DNS results with experimental (exp.) data (Roghelia *et al.* 2017*b*) for the surface pressure coefficient and wall Stanton number along the model's line of symmetry. (*b*) Comparison of the boundary layer profiles from the DNS data with the similarity solution of the boundary-layer equations. The vertical coordinate represents the non-dimensional wall-normal distance $\eta = y/x\sqrt{Re_x}$.

magnitude is very small. Furthermore, the laminar boundary layer profiles upstream of separation are compared with the theoretical solution of the compressible flat plate boundary layer equations (Anderson 2006) in figure 2(*b*). Despite the slight differences resulting from the viscous interaction at the leading edge, which results in a streamwise pressure gradient, the achieved agreement is very good.

The grid independence is discussed in the following. Figure 3 provides the comparison of the three-dimensional simulation results. Figures 3(*a*) and 3(*b*) show the instantaneous distribution of the wall Stanton number for cases G1 and G2, respectively. The positions where the skin friction coefficient ($C_f$) is zero are also shown to highlight the separation and reattachment positions. As the streamwise streaks are non-uniformly distributed in the spanwise direction, their wavelengths vary between $4 \sim 6$ mm, which is consistent with the experimental results (Roghelia *et al.* 2017*b*). Furthermore, the standard deviation of the spanwise Stanton number variation at $x/L = 1.5$ with respect to the spanwise-averaged value is 30 % for both cases. Therefore, the comparable wavelength and amplitude between cases G1 and G2 indicates that the spanwise resolution for case G1 is sufficient to resolve the streamwise streaks, and the chosen spanwise model length has no significant influence on the results. Figure 3(*c*) shows the streamwise distribution of the spanwise-averaged wall Stanton number and surface pressure coefficient for both cases. The almost identical pressure distribution indicates the same positions of separation and reattachment. In fact, the deviation of the separation bubble length is less than 1 %. The minor discrepancy for the Stanton number can be attributed to the difference in the spanwise model length. In summary, the excellent agreement between the DNS results and the experimental data as well as the theoretical predictions confirms the reliability of the DNS solver, and the mesh resolution for case G1 is sufficient to resolve the flow phenomenon of interest.

## 3. Flow establishment and global instability

### 3.1. *Flow establishment*

To characterise the growth of three-dimensionality with respect to the base flow obtained from the two-dimensional simulation, we consider the temporal evolution of the spanwise
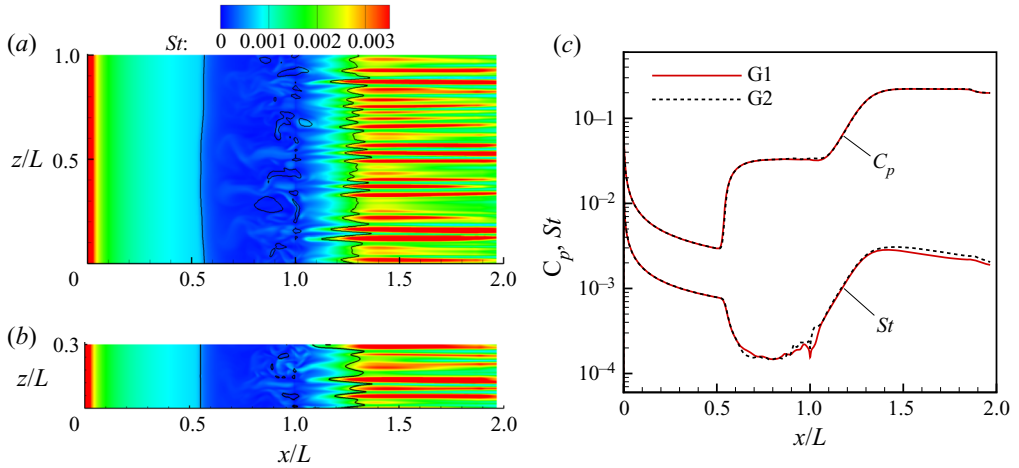
Figure 3. Comparison of the DNS results for the two mesh cases. Instantaneous ($tu_\infty/L = 66$) distribution of the wall Stanton number is shown for (*a*) case G1 and (*b*) case G2. Black lines denote isolines of zero skin friction coefficient. (*c*) Streamwise distribution of the spanwise-averaged surface pressure coefficient and wall Stanton number at the same instant of time.

velocity component ($w/u_\infty$) in the flow field. In particular, the absolute value of the spanwise velocity in a $z$–$y$ plane is calculated as follows:

$$\sigma_w = \sqrt{\frac{1}{N_y N_z} \sum_{j=1}^{N_y} \sum_{k=1}^{N_z} (w/u_\infty)_{j,k}^2}, \tag{3.1}$$

where $N_y$ and $N_z$ are the number of grid points in the wall-normal and spanwise directions, respectively. Figure 4 shows the temporal evolution of $\sigma_w$ at $x/L = 1.04$. As seen, the initialised random value damps to the order of $10^{-5}$ at the very beginning ($tu_\infty/L < 1$). Then, an exponential growth stage takes place and ends at approximately $tu_\infty/L = 12$. Subsequently, the spanwise velocity grows progressively until reaching the asymptotic level at approximately $tu_\infty/L = 50 \sim 60$. The reason for showing $\sigma_w$ at $x/L = 1.04$ is given as follows.

By examining $\sigma_w$ at all $x$ positions, it is found that the largest quantity occurs at $x/L = 1.04$ during the exponential growth stage. The streamwise distribution of $\sigma_w$ at $tu_\infty/L = 9$ and 12 is presented in figure 5, where these instants of time have been chosen exemplarily for the exponential growth stage. Note that the separation bubble is located at $0.59 < x/L < 1.26$. Therefore, the three-dimensionality is mainly confined in the separation bubble at the exponential growth stage.

In the following, the flow features during the flow establishment period are analysed. Figure 6 shows the distribution of spanwise velocity on the $x$–$y$ plane at $z/L = 0.46$ and on the $z$–$y$ plane at $x/L = 1.04$ for $tu_\infty/L = 9$. Consistent with figure 5, the spanwise velocity perturbations (three-dimensionality) are mainly generated in the separation bubble. In addition, a periodic spanwise flow pattern is found in the separation bubble (see figure 6*b*). On average, the spanwise wavelength of this flow pattern is approximately 6.7 mm. It will be shown later that the global instability with respect to the base flow is responsible for this spanwise modulation. After experiencing the exponential growth stage, the flow in the separation bubble is going to saturate, and the regular spanwise modulation is modified significantly. Figure 7 presents the distribution of spanwise velocity at $tu_\infty/L = 51$
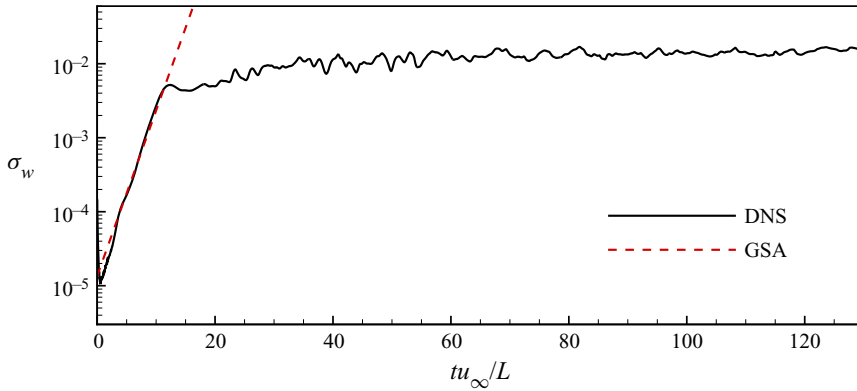
Figure 4. Temporal evolution of $\sigma_w$ (from (3.1)) at $x/L = 1.04$. The red dashed line represents the growth rate predicted by GSA, which is shown later.
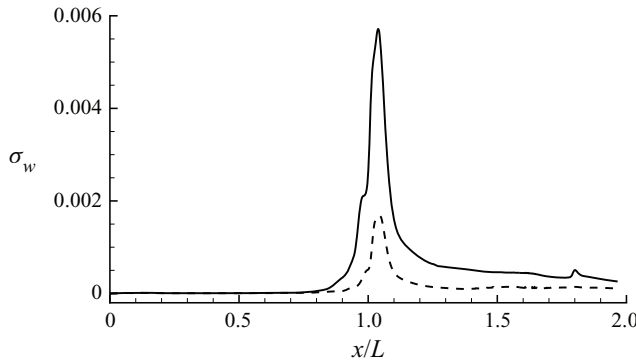


Figure 5. Streamwise distribution of $\sigma_w$ (from (3.1)) at $tu_\infty/L = 9$ (dashed line) and 12 (solid line).
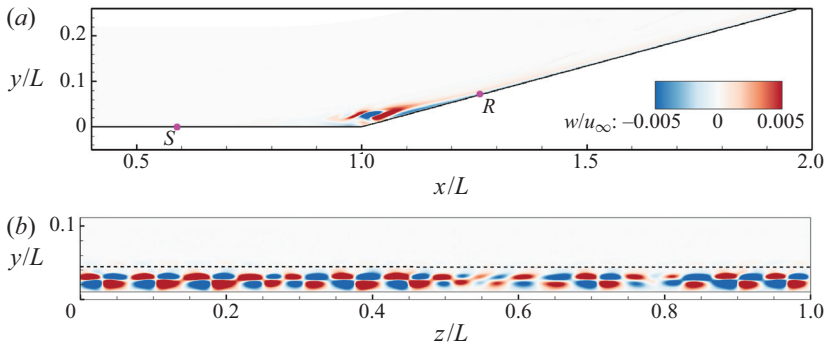


Figure 6. Instantaneous distribution of spanwise velocity on (*a*) the $x$–$y$ plane at $z/L = 0.46$ and (*b*) the $z$–$y$ plane at $x/L = 1.04$ at $tu_\infty/L = 9$. Here $S$ and $R$ denote the separation and reattachment positions, respectively. Dashed line indicates the centre position of the shear layer (the position for maximum velocity gradient $\partial u/\partial y$).

and 100. It is apparent that the spanwise velocity distribution is generally irregular and different at these two instants of time. It implies that the saturated flow is unsteady, as shown below.

Figure 8 presents six instantaneous distributions for the wall Stanton number. The isolines of zero skin friction coefficient are shown to highlight the separation and
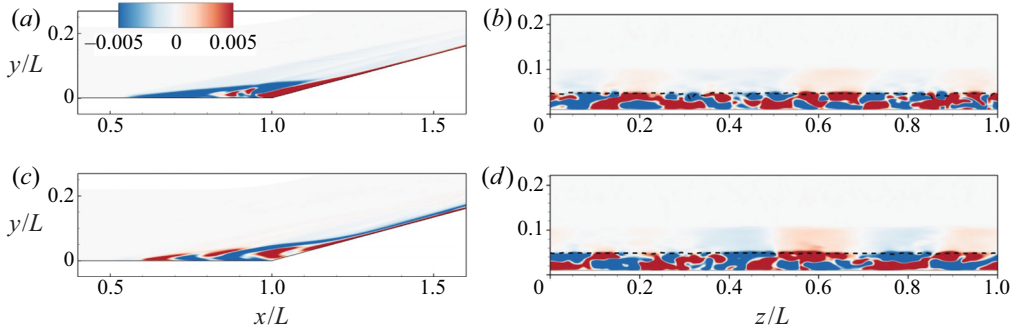
**912** A3-9

Figure 7. Instantaneous distribution of spanwise velocity on (*a*,*c*) the *x*–*y* plane at $z/L = 0.5$ and (*b*,*d*) the *z*–*y* plane at $x/L = 1.04$ for the time instants of (*a*,*b*) $tu_\infty/L = 51$ and (*c*,*d*) $tu_\infty/L = 100$. The dashed line indicates the centre position of the shear layer.

reattachment positions. At $tu_\infty/L = 0$ (figure 8*a*), the initial flow field is a simple extrapolation of the two-dimensional converged solution. At $tu_\infty/L = 9$ (figure 8*b*), the flow is undergoing the exponential growth stage, and a spanwise variation of surface heat flux occurs inside and downstream of the separation bubble. Distinct streamwise heat flux streaks can be observed in the vicinity of flow reattachment at $tu_\infty/L = 21$ (figure 8*c*), whose spanwise wavelength is approximately 3.4 mm. Subsequently, at $tu_\infty/L = 51$, 100 and 120, the surface heat flux streaks are non-uniformly distributed in spanwise direction, which is consistent with the experimental observations for naturally developed streaks (Simeonides & Haase 1995; Chuvakhov *et al.* 2017; Roghelia *et al.* 2017*a*,*b*). The streak pattern at these three instants of time looks similar but not identical, indicating an unsteady behaviour of the flow over the ramp. It is further noted that for the fully developed flow, the reattachment line becomes meandering, indicating a three-dimensional flow reattachment. Note also that the size of the separation bubble is slightly increased due to the occurrence of the three-dimensionality.

To identify the fluctuation of the surface heat flux, the temporal history of the wall Stanton number at $x/L = 1.5$ and $z/L = 0.5$ is clearly presented in figure 9. Interestingly, the wall Stanton number starts to fluctuate at approximately $tu_\infty/L = 12$, which corresponds to the end of the exponential growth stage. This fluctuation confirms the presence of unsteady heat flux streaks on the wall, as demonstrated in figure 8. On the basis of the above analyses, it is concluded that after an initial exponential growth of three-dimensionality and a subsequent flow saturation stage, the flow field reaches the quasi-steady state prior to $tu_\infty/L = 60$. Therefore, it is appropriate to study the flow unsteadiness for the time period of $tu_\infty/L = 60$ to approximately 130, because this period of time covers a sufficient number of fluctuations (see figure 9). Before characterising the flow unsteadiness, the evolution of three-dimensionality in the flow field is further explained by performing a GSA.

### 3.2. *GSA with respect to the two-dimensional base flow*

The present DNS results show that three-dimensionality occurs without any external forcing disturbances, which indicates that the two-dimensional ramp flow under the current condition is intrinsically unstable to three-dimensional perturbations. It is therefore of interest to perform a GSA to facilitate a better understanding of the formation and development of the three-dimensionality.
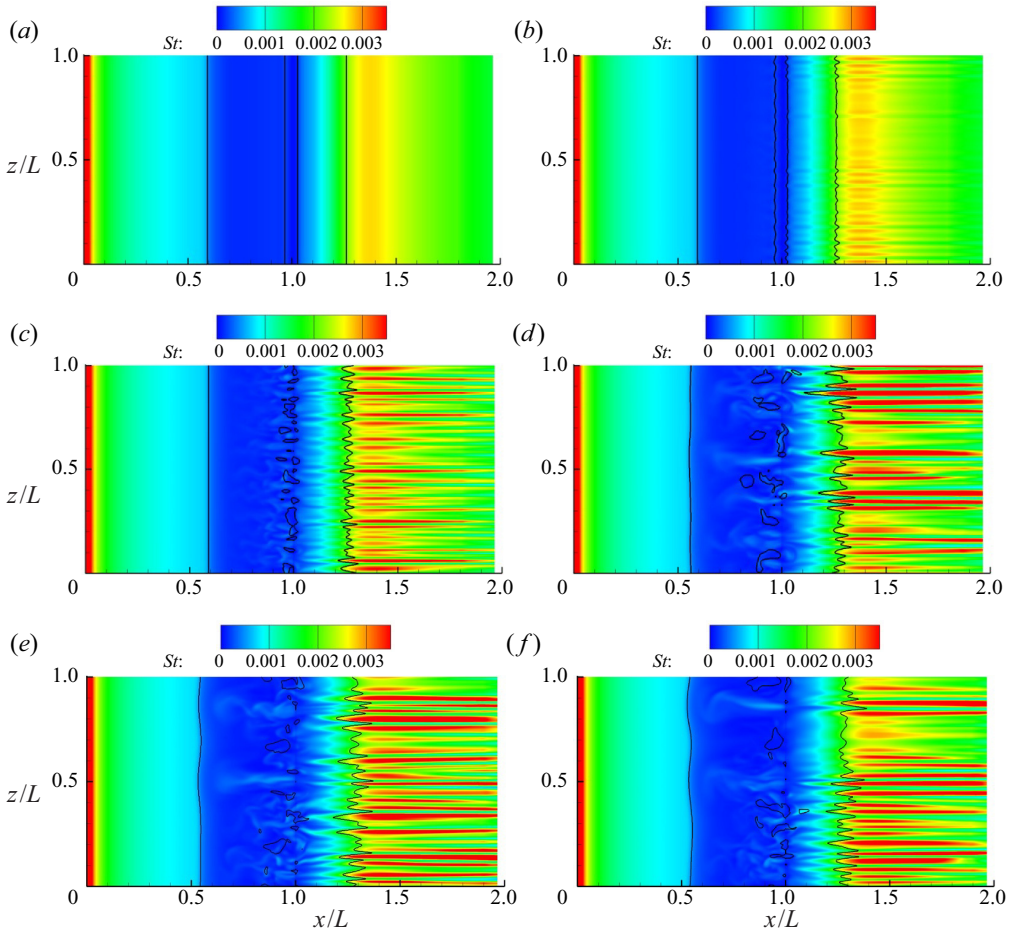
**912** A3-10

Figure 8. Instantaneous distribution of wall Stanton number at (*a*) $tu_\infty/L = 0$, (*b*) $tu_\infty/L = 9$, (*c*) $tu_\infty/L = 21$, (*d*) $tu_\infty/L = 51$, (*e*) $tu_\infty/L = 100$ and (*f*) $tu_\infty/L = 121$. Black solid lines denote isolines of $C_f = 0$. The flow is from left to right.
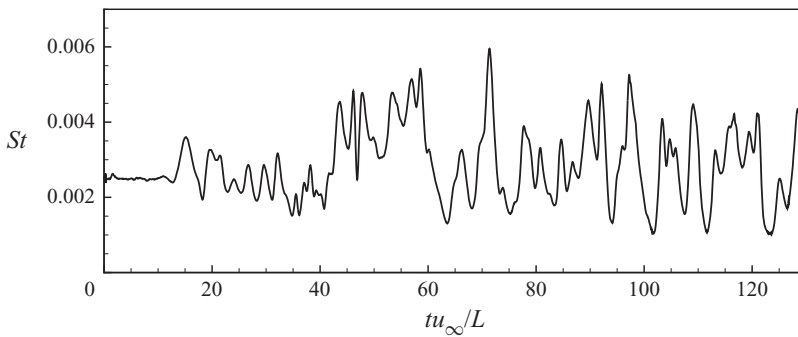


Figure 9. Temporal history of the wall Stanton number at $x/L = 1.5$ and $z/L = 0.5$.

**912** A3-11

To this end, a global stability solver is constructed with the linearised compressible Navier–Stokes equations written in the conservative form and discretised using a second-order finite-volume method. Specifically, a modified Steger–Warming scheme (MacCormack 2014) is combined with a central scheme using an improved Ducros shock sensor (Hendrickson, Kartha & Candler 2018) to compute the inviscid Jacobians. The flux-vector splitting method is activated near discontinuities to eliminate numerical noise, whereas the central scheme is used in smooth regions to ensure adequate numerical accuracy. Details of the inviscid and viscous Jacobians can be found in Sidharth *et al.* (2018).

The two-dimensional converged solution is used as the base flow. If we further assume that the three-dimensional perturbations are periodic in the $z$-direction, the vector of the perturbed conservative variables $U'$ can be expressed as

$$U'(x, y, z) = \hat{U}(x, y) \exp[-i(\omega_r + i\omega_i)t + i\beta z] + \text{complex conjugate}, \qquad (3.2)$$

where $\hat{U}$ is the eigenfunction, $\omega_r$ is the angular frequency, $\omega_i$ is the growth rate and $\beta$ is the spanwise wavenumber. A mode is unstable when $\omega_i > 0$, and stable when $\omega_i < 0$. Here $\omega_r = 0$ indicates a stationary mode, whereas $\omega_r \neq 0$ represents an oscillatory mode. The corresponding frequency and spanwise wavelength are defined by

$$f = \frac{\omega_r}{2\pi}, \quad \lambda_z = \frac{2\pi}{\beta}. \qquad (3.3a,b)$$

The eigenvalue problem resulting from substituting (3.2) into the linearised Navier–Stokes equations is solved using the implicit restarted Arnoldi method implemented in ARPACK (Sorensen *et al.* 1996–2008). The shift–invert approach is adopted to efficiently explore the eigenvalue spectra, in which the inversion step is calculated using the lower–upper decomposition implemented in SuperLU (Li *et al.* 1999). Note that periodicity in the $z$-directions is implemented analytically, which means that the Jacobians are complex matrices.

Four unstable modes have been identified with the corresponding growth rates and frequencies plotted in figure 10 as a function of $\lambda_z$. The most unstable mode (mode 1) occurs at $\lambda_z/L = 0.066$. A closer examination of the spectrum reveals that mode 1 is stationary for $\lambda_z/L < 0.105$ and becomes oscillatory for larger $\lambda_z$. By contrast, modes 2 and 3 are oscillatory with their growth rates peaking at $\lambda_z/L = 0.070$ and 0.079, respectively. Mode 4 is a stationary mode, which is most unstable at $\lambda_z/L = 0.349$. Modes 1 and 4 essentially belong to the same branch of eigenvalues.

Figure 11 shows the eigenvalue spectrum at $\lambda_z/L = 0.066$. Grid independence was verified by increasing the grid nodes in the $x$- and $y$-directions simultaneously by a factor of 1.5. At this spanwise wavelength, mode 1 is stationary, indicating that the perturbation amplitudes increase monotonically with time until nonlinear saturation. The non-dimensional frequencies of modes 2 and 3 are 0.224 and 0.579, respectively.

Concerning the DNS results, the flow behaviour is well predicted by the GSA. In the GSA, small-amplitude perturbations are assumed to grow exponentially in time (Theofilis 2011; Sidharth *et al.* 2018). By comparing the growth rate of the most unstable mode (mode 1) with the growth of spanwise velocity perturbation ($\sigma_w$) resulting from DNS in figure 4, it is obvious that after an initial adaption before $tu_\infty/L = 3$, the growth rate resulting from DNS agrees well with the GSA prediction. It indicates that the growth of three-dimensionality prior to $tu_\infty/L = 12$ is dominated by the stationary global unstable mode. Another piece of direct evidence can be found in figure 6(*b*), where the spanwise
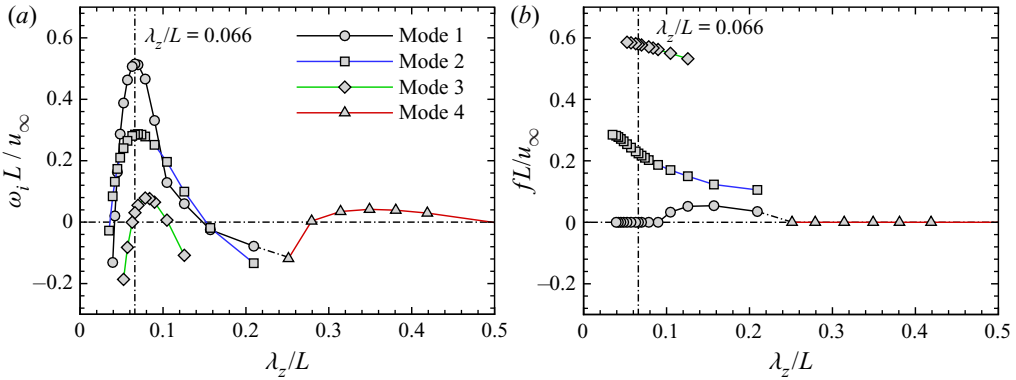
Figure 10. (*a*) Growth rates and (*b*) frequencies of the unstable modes as a function of spanwise wavelength $\lambda_z$.
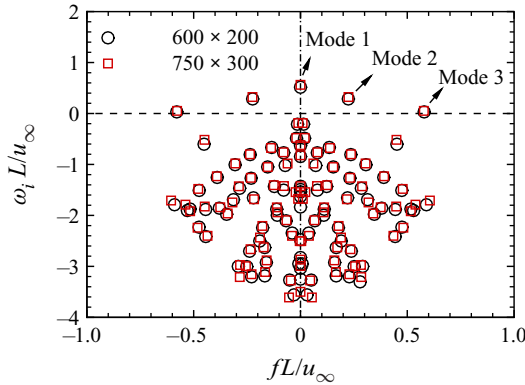


Figure 11. Eigenvalue spectra at $\lambda_z/L = 0.066$ obtained using different grids.

wavelength of the periodic flow pattern coincides with the wavelength of mode 1 ($\lambda_z/L = 0.066$).

Although the growth rate of modes 2 and 3 is smaller than that of mode 1, hints regarding their presence in the DNS results can be found by performing a fast Fourier transform for the spanwise velocity field on a wall-parallel plane ($y_n/L = 0.0018$) at $tu_\infty/L = 9$. Figure 12 shows the resulting power spectral density (PSD) contour as a function of the non-dimensional spanwise wavelength and streamwise location. A dominant spanwise wavelength can be found near $\lambda_z/L \approx 0.066$ corresponding to mode 1. Mode 2 cannot be clearly distinguished from mode 1 due to their similar wavelengths. The PSD concentrated at $\lambda_z/L \approx 0.09$ corresponds to mode 3. At this instant, DNS also shows the second harmonics of modes 1–3 with $\lambda_z/L$ ranging from 0.033 to 0.04. It is interesting to note that the streamwise surface heat flux streaks at $tu_\infty/L = 9$ and 21 (see figure 8*b*,*c*) exhibit a wavelength of $\lambda_z/L \approx 0.033$, which is consistent with the second harmonic of the wavelength of mode 1. Since the early growth of the three-dimensionality is dominated by mode 1, the footprints of modes 2–4 may be better observed at the later growth stage.

At the late stage (e.g. after $tu_\infty/L = 60$), the saturated flow has already modified the base flow. However, if the base flow is not far beyond the bifurcation point, the wavelength of the streaks obtained by DNS will match that predicted by GSA (Sidharth *et al.* 2017, 2018). As seen in figure 8(*d*–*f*), the wavelength of the streaks varies in the vicinity of
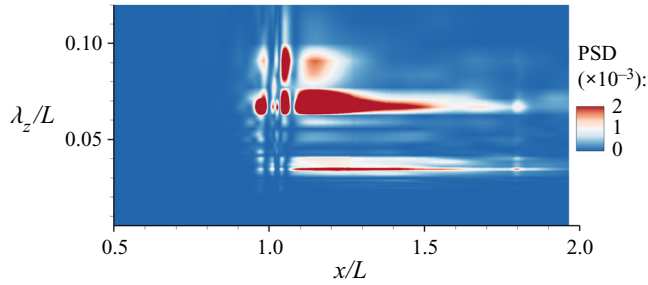
Figure 12. The PSD of the spanwise velocity on a wall-parallel plane ($y_n/L = 0.0018$) obtained from DNS at $tu_\infty/L = 9$.
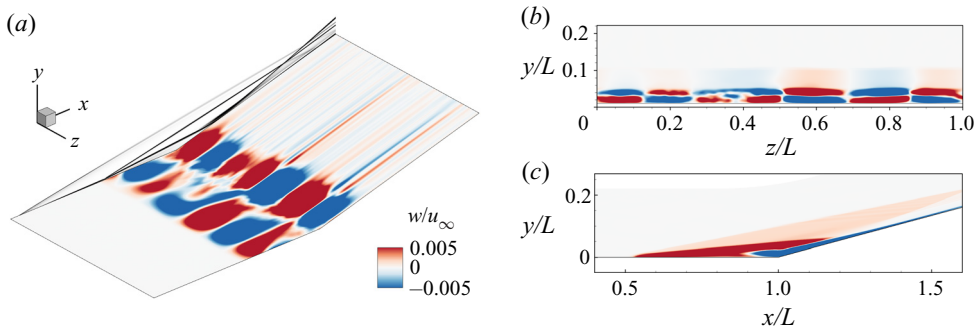


Figure 13. Time-averaged distribution of the spanwise velocity component at different planes: (*a*) wall-parallel plane at $y_n/L = 0.009$; (*b*) $z$–$y$ plane at $x/L = 1.04$; (*c*) $x$–$y$ plane at $z/L = 0.6$. The density gradient at $z/L = 0$ is shown in panel (*a*) to highlight the position of the separation bubble.

$\lambda_z/L \approx 0.04$, which is close to the second harmonics of modes 1–3. Furthermore, the time-averaged flow (averaged from $tu_\infty/L = 60$ to 130) exhibits a spanwise wavelength of $\lambda_z/L \approx 0.33$, as shown in figure 13. Surprisingly, this wavelength agrees well with the most unstable wavelength of mode 4. Note that mode 4 is a stationary mode, and hence it can be better extracted from the time-averaged flow. Note also that the wavelength of the stationary mode 1 is very close to that of the oscillatory modes 2–3. Thus, mode 1 is not distinguished in the time-averaged flow. It is seen in figure 13 that the large-scale spanwise periodicity is confined in the separation bubble. This flow structure is typical of vortical cells moving away from the wall at the centre of a vortex pair (upwash) or towards the wall at the position between two vortex pairs (downwash). In summary, footprints of the global modes revealed by the GSA are well observed in the DNS data.

Figure 14 shows the contours of the real part of the spanwise velocity perturbation $\hat{w}/u_\infty$ for modes 1–4 at their most unstable wavelengths (i.e. $\lambda_z/L = 0.066, 0.070, 0.079$ and $0.349$). Note that a sponge layer was implemented from $x/L = 1.9$ to damp the perturbations to zero and allow the use of a simple extrapolation condition at the outflow boundary (Mani 2012). For mode 1, most of the perturbations are confined in the downstream half of the separation region, which stretch farther downstream through the reattaching shear layer. It is indicated that these two flow regions are closely coupled with each other. This mode shape is identical to the flow structure captured by the DNS (see figure 6*a*). A similar eigenfunction was also reported by Sidharth *et al.* (2017) for a heated ramp flow. By contrast, modes 2–4 are present in the entire separation region. Notably, modes 2 and 3 exhibit streamwise periodicity in the upstream half of the
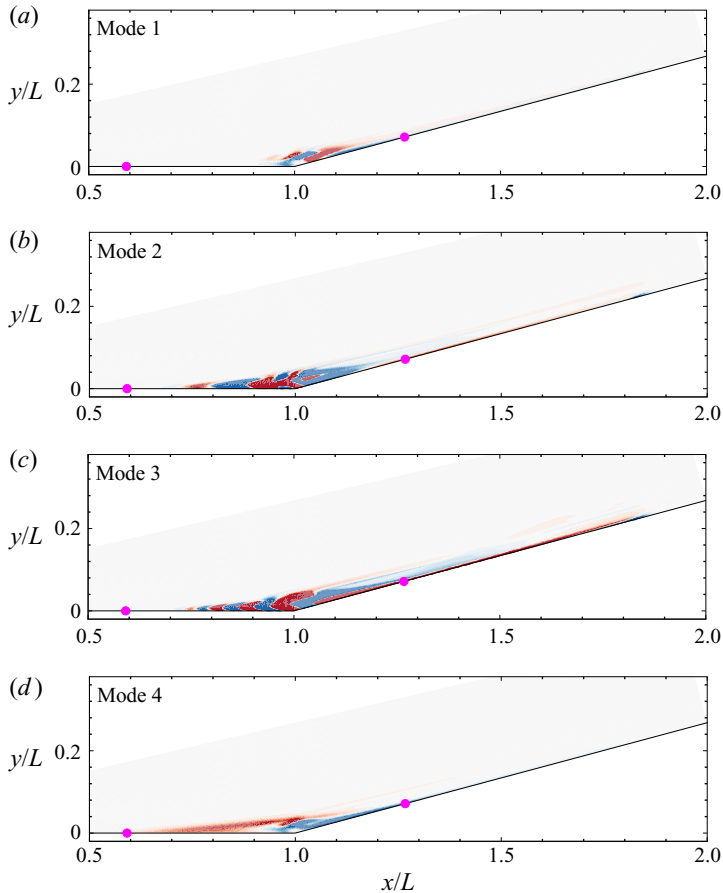
**912** A3-14

Figure 14. Real parts of the spanwise velocity perturbation $\hat{w}/u_\infty$ for (*a*) mode 1 at $\lambda_z/L = 0.066$; (*b*) mode 2 at $\lambda_z/L = 0.070$; (*c*) mode 3 at $\lambda_z/L = 0.079$; (*d*) mode 4 at $\lambda_z/L = 0.349$. The separation and reattachment points are marked with circles.

separation bubble, indicating travelling spanwise oblique perturbations associated with temporal oscillations (Sidharth *et al.* 2018).

## 4. Unsteady features downstream of reattachment

Due to the presence of global unstable modes (both stationary and oscillatory), the saturated flow exhibits complicated unsteady features. In the following, the flow unsteadiness near and downstream of reattachment is studied based on the DNS data.

### 4.1. *Spatio-temporal distribution of the surface heat flux downstream of reattachment*

For illustration of the unsteady surface heat flux, an animation showing wall Stanton number snapshots between $tu_\infty/L = 60$ and $tu_\infty/L = 130$ is available in the supplementary movie available at https://doi.org/10.1017/jfm.2020.1093. It is seen that the position, intensity and thickness of the streaks vary irregularly with time, which clearly demonstrates the unsteady behaviour of the surface heat flux. Moreover, some streaks are emerging, while some others disappear. The movement of the streaks seems to have a
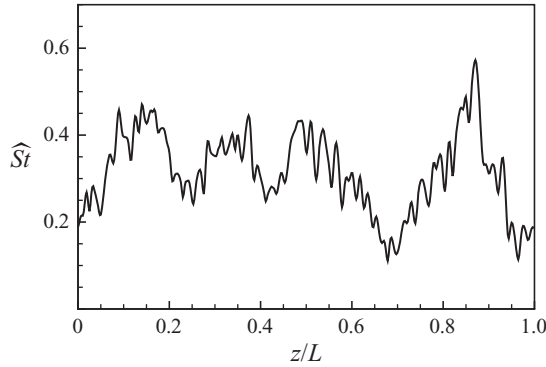
Figure 15. Relative standard deviation of the wall Stanton number for all spanwise positions at $x/L = 1.5$.

connection to the movement of the reattachment line. In the following, statistical analyses are performed to characterise the unsteady behaviour of the surface heat flux.

Considering the temporal fluctuation of the surface heat flux downstream of reattachment, its relative standard deviation can be determined as follows:

$$\widehat{St} = \frac{\sqrt{\dfrac{1}{N}\sum_{i=1}^{N}(St_i - \overline{St})^2}}{\overline{St}}, \tag{4.1}$$

where $\overline{St}$ denotes the time-averaged value, and $N$ is the number of sampling points. The relative standard deviation $\widehat{St}$ for all spanwise positions at $x/L = 1.5$ is presented in figure 15. It is clear that $\widehat{St}$ is not constant in the spanwise direction. We note that this spanwise variation is related to the coherent structure shown in figure 13. For example, the strongest fluctuation has a $\widehat{St}$ value of 57 % and is located at $z/L = 0.87$, corresponding to the upwash position in a vortex pair. However, the lowest $\widehat{St}$ is found at $z/L = 0.68$, corresponding to the downwash position between two vortex pairs. This result indicates a direct influence of the separation bubble flow on the downstream heat flux fluctuation, which suggests that the unsteadiness in the reattached flow may be traced back to the separation bubble.

To identify a possible transport direction of the flow unsteadiness, a two-point spatio-temporal correlation is employed to evaluate the fluctuation quantities of the wall Stanton number ($St' = St - \overline{St}$),

$$R_{nm}(\tau) = \frac{\overline{St'_n(t) \cdot St'_m(t+\tau)}}{\sqrt{\overline{St'^2_n}} \cdot \sqrt{\overline{St'^2_m}}}, \tag{4.2}$$

where the subscript $n$ denotes the reference point $x/L = 1.5$, $z/L = 0.5$; $m$ corresponds to the position varying in streamwise or spanwise direction; and $\tau$ is the time delay.

Figure 16 shows the calculated correlation maps. It is apparent that a strong correlation exists in the streamwise direction, whereas the correlation in the spanwise direction is quite weak. It means that the primary propagation direction of the unsteadiness is in the streamwise direction. The linear slope of the main structure shown in figure 16(*a*) by the solid black line indicates the travelling speed of the unsteadiness, which is evaluated approximately by $0.7u_\infty$.
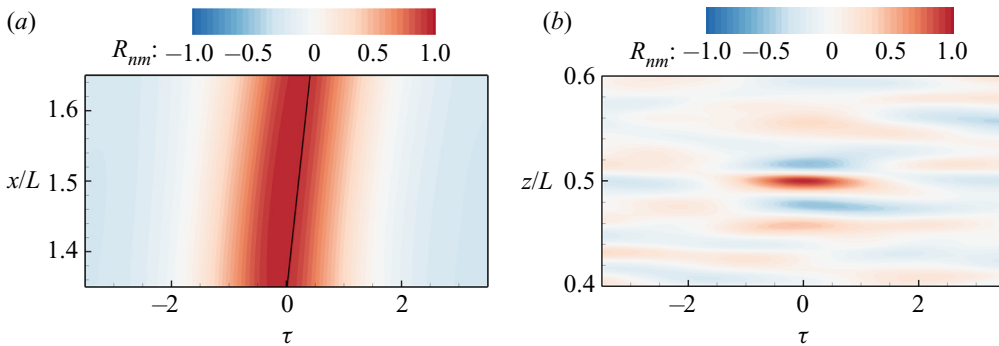
Figure 16. Two-point temporal correlation maps for the wall Stanton number in (*a*) the streamwise direction and (*b*) the spanwise direction. Reference point is located at $x/L = 1.5$, $z/L = 0.5$.
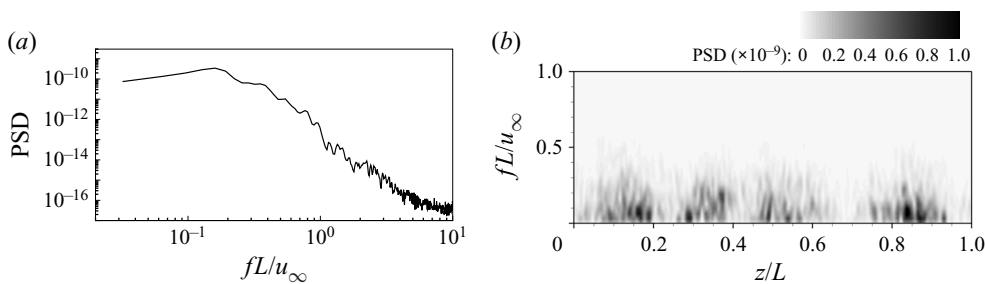


Figure 17. (*a*) Power spectral density of the wall Stanton number signal at $x/L = 1.5$ and $z/L = 0.5$. (*b*) Power spectral density map for all spanwise positions at $x/L = 1.5$.

In terms of the fluctuation frequency, the PSD of the wall Stanton number signal shown in figure 9 is firstly considered. Note that the calculation is performed for the time period of $tu_\infty/L = 60 \sim 130$ with a sampling frequency of 0.57 MHz. Welch's method (Welch 1967) is employed for the spectral estimation with seven segments and 50 % overlap. A Hamming window is used for weighting the data on each segment prior to fast Fourier transform processing. The above setting yields the length of an individual segment being $17.5L/u_\infty$. The resulting PSD is shown in figure 17(*a*). It is seen that the surface heat flux signal has a broadband low-frequency feature, and the dominant non-dimensional frequencies ($fL/u_\infty$) are lower than 1 and approximately centred at $fL/u_\infty = 0.15$.

Figure 17(*b*) provides the PSD contour for the wall Stanton number by considering all spanwise positions at $x/L = 1.5$. The low-frequency characteristic holds at all spanwise positions, though a spanwise variation of amplitude exists. In general, groups of high amplitude are present at certain spanwise positions. This is consistent with the spanwise variation of the relative standard deviation shown in figure 15. It is noted that the frequencies of modes 2 and 3 found by the previous GSA are 0.224 and 0.579, respectively, which are covered by the broadband spectrum for the wall Stanton number.

## 4.2. *Unsteady flow reattachment*

Since the flow reattachment directly influences the downstream reattached flow, it is necessary to study the unsteadiness near reattachment. Figure 18 shows the temporal history of the spanwise-averaged reattachment position and the particular reattachment
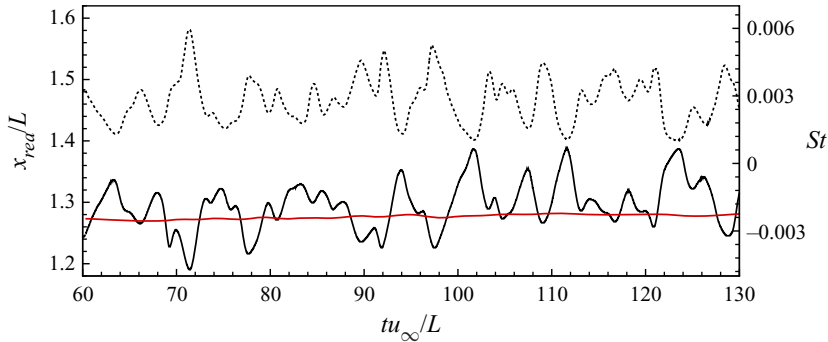
**912** A3-17

Figure 18. Temporal history of reattachment positions in comparison with wall Stanton number. The black solid line corresponds to the reattachment position for the plane of symmetry ($z/L = 0.5$) and the red solid line to the spanwise-averaged reattachment position. The dashed line is the wall Stanton number signal shown in figure 9.

position on the plane of symmetry ($z/L = 0.5$), in comparison with the downstream wall Stanton number signal. Unlike the pulsation of the reattachment point at $z/L = 0.5$, the spanwise-averaged reattachment point is nearly invariant, indicating a steady state for the spanwise-averaged separation bubble. It should be mentioned that the spanwise-averaged separation position also maintains temporarily invariant. This can be observed in the supplementary animation. Therefore, the well known breathing of the separation bubble in turbulent SWBLI (Priebe & Martín 2012; Clemens & Narayanaswamy 2014; Pasquariello, Hickel & Adams 2017) is absent here. Note however, that the separation bubble size in the present case is much larger than those in the turbulent flow.

By comparing the temporal distribution of the reattachment position at $z/L = 0.5$ and the downstream wall Stanton number, a generally opposite trend is apparent in figure 18; when the reattachment position moves downstream, the Stanton number decreases, and *vice versa*. This opposite trend reveals a close link between flow reattachment and the downstream surface heat flux streaks, which can be explained by showing the streamline topology at reattachment. For the flow reattachment with accompanying streamwise streaks, Ginoux (1971) and Inger (1977) proposed a three-dimensional topology of the limiting streamline near reattachment, which was further improved by Cao *et al.* (2019a) and Kavun *et al.* (2019). As shown in figure 19(a), a series of singularities (nodes and saddle points) are distributed along the reattachment line, and nodes are located upstream of saddle points, which is confirmed by the present DNS results (see figures 8 and 19b). In addition, this streamline topology is similar to that induced by global instability (Sidharth *et al.* 2018). This similarity suggests a continuous influence of global instability on the saturated flow. Downstream of a saddle point, the flow is forced to coalesce, resulting in a lift-up effect of the reattached boundary layer. As a result of a three-dimensional reattaching shear layer and this flow topology at reattachment, a hot streak (large *St*) is always located downstream of a node and a cold streak (small *St*) downstream of a saddle point. Therefore, the pulsation of the reattachment position is accompanied by a variation of the downstream surface heat flux. In addition, the spectra of the reattachment position signal are the same as that of the wall Stanton number due to its opposite behaviour.

The above analyses revealed the unsteady behaviour of the streamwise heat flux streaks and their connection to the flow reattachment. It is shown that the surface heat flux are coupled with the pulsation of reattachment line, oscillating at relatively low frequencies. These results indicate that the unsteadiness originates from the three-dimensional
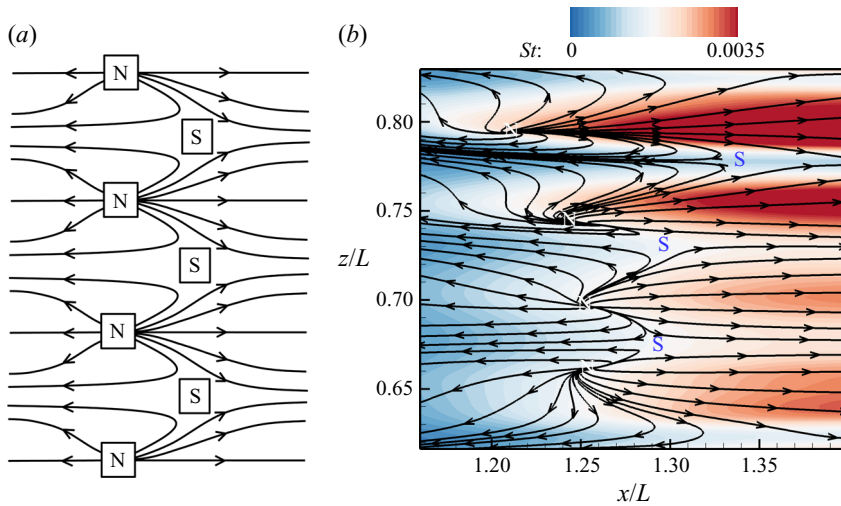
Figure 19. (*a*) Streamline topology near reattachment proposed by Cao *et al.* (2019*a*). (*b*) Streamlines on a near-wall plane ($y_n/L = 0.0008$) embedded in the wall Stanton number contour at $tu_\infty/L = 100$. Here N and S denote nodes and saddle points, respectively.

separation bubble. As revealed by the GSA performed earlier, two oscillatory global modes exist in the separation bubble with respect to the two-dimensional base flow. Hence, one may conceive that the unsteadiness in the saturated separation bubble flow is triggered by the global instability. In what follows, the separation bubble flow with respect to its saturated state is examined in an attempt to uncover its instability.

## 5. Dynamic mode decomposition of the separation bubble flow

Dynamic mode decomposition, developed by Schmid (2010), is a data processing algorithm that extracts coherent spatial structures sharing the same temporal frequency. The extracted dynamic modes are a reduced-order representation of the underlying flow field. The resulting eigenvalues $\mu_i$ encode the temporal frequency and growth/decay rate of the DMD modes. As a post-processing procedure for selecting DMD modes and eigenvalues, sparsity-promoting dynamic mode decomposition (SPDMD) has recently been developed by Jovanović, Schmid & Nichols (2014) to achieve a desirable trade-off between the quality of approximation and the number of modes that are used to approximate the given flow fields. It facilitates the selection of the dynamically most important modes of the underlying flow field. For the detailed algorithm of processing the mode decomposition and selection please refer to Schmid (2010) and Jovanović *et al.* (2014).

We subsequently perform DMD for the fully saturated separation bubble flow. In particular, the instantaneous fields of the spanwise velocity component ($w/u_\infty$) for the plane of symmetry are decomposed. The database, extracted from $tu_\infty/L = 100 \sim 130$, includes 1000 snapshots which are equispaced by a time interval of $\Delta tu_\infty/L = 0.03$. This yields a frequency resolution of $0.033 \le fL/u_\infty \le 16.7$. The spectrum of the eigenvalues obtained from the standard DMD algorithm is shown in figure 20(*a*). The resulting modes are symmetric about the real axis due to the real-valued input data. It is apparent that almost all eigenvalues reside on the unit circle. This is expected for a statistically stationary system as the growth/decay rate is nearly zero.
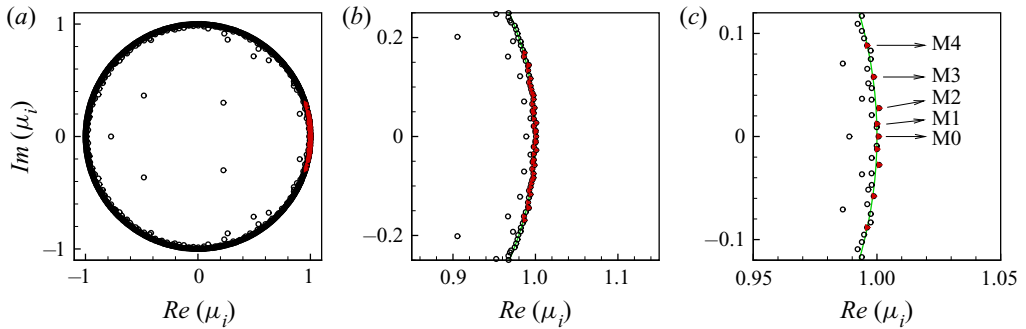
Figure 20. Spectrum of the eigenvalues obtained from the standard DMD (circles) and the modes selected by SPDMD (red triangles) for a subset of (*a*) $N_{sp} = 36$, (*b*) $N_{sp} = 22$ and (*c*) $N_{sp} = 5$. The green line represents the unit circle.

The SPDMD algorithm is processed to facilitate the selection of dynamically important modes. The number of the retained DMD modes ($N_{sp}$) resulting from the SPDMD is controlled by a user-defined parameter, which is a measure of preference between approximation quality and solution sparsity (Jovanović *et al.* 2014). It is found that to reduce the performance loss to 16 %, a subset of $N_{sp} = 36$ modes has to be included. These modes nearly cover all the modes in the low-frequency region, as shown in figure 20(*a*). The associated frequencies ($fL/u_\infty$) for these modes range from 0 to 1.6. This result indicates that the considered unsteady flow has a broadband spectrum. This is consistent with the PSD analysis for the downstream flow (see, for example, figure 17). If the number of selected modes are reduced to 22 (figure 20*b*), 50 % of the total energy is covered and the associated frequency range is $0 \sim 0.9$. The five most energetic modes shown in figure 20(*c*) cover 20 % of the energy among all the modes. These modes are labelled as M0, M1, M2, M3 and M4. The associated frequencies are $fL/u_\infty = 0$, 0.07, 0.15, 0.30 and 0.47, respectively. It is noted that these modes yield a typical representation of the considered data sequence. By examining the mode shape for all the 36 modes in figure 20(*a*), we found that they share similar flow structures compared with modes M0–M4.

Figure 21 shows the real part of modes M0, M1, M3 and M4. The mode M0 has a zero frequency and hence is related to the time-averaged flow. For the other modes, the shown contours represent the fluctuations $w'/u_\infty$ associated with a particular frequency. It is apparent that streamwise periodic structure exists in the separation bubble flow. This structure is consistent with the shape of modes 2 and 3 shown in figure 14(*b*,*c*) as well as that of the oscillatory unstable mode found by Sidharth *et al.* (2018). Additionally, the length scale of the periodic structure decreases with increasing frequency. It is noted that these structures are mainly located at the upstream half of the recirculation bubble. The core of the recirculation bubble is located at $x/L = 1.04$.

Furthermore, figure 22 illustrates the position of the periodic structure with respect to the shear layer. Specifically, two isolines of the streamwise velocity ($u/u_\infty = 0.1$ and 0.9) are utilised to cover the main part of the shear layer in figure 22(*a*). Then, the two lines are embedded in the contour for mode M4, as shown in figure 22(*b*). Note that for a better visualisation, the scales of the horizontal and vertical coordinates are set to be independent. It is clear that the shear layer is able to entrain the periodic structure downstream. This shear layer entrainment is the key to connect the unsteadiness of the separation bubble flow to the reattached flow, which causes the pulsation of reattachment position and the low-frequency heat flux fluctuation downstream of reattachment. In fact,
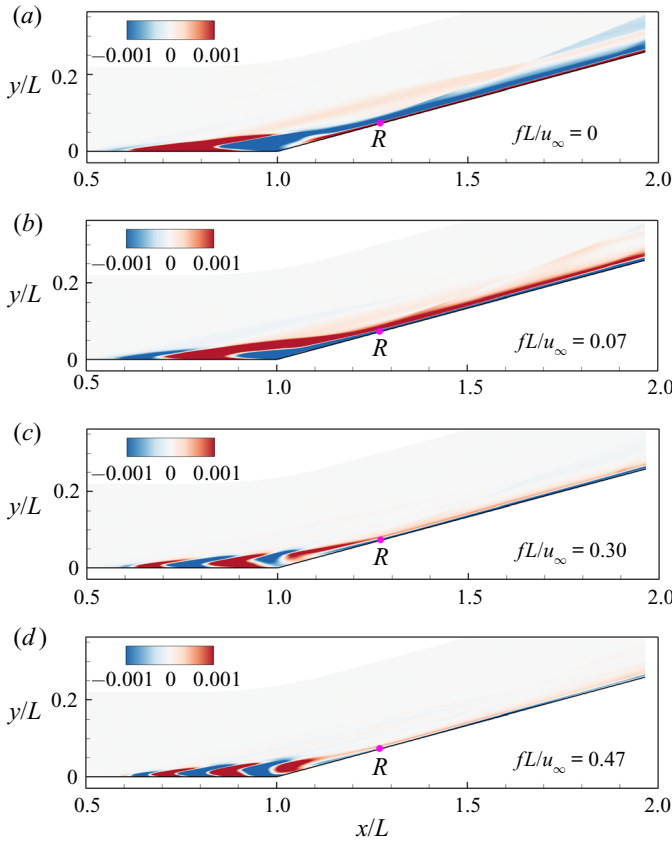
Figure 21. The DMD modes visualised by contours of spanwise velocity component ($w/u_\infty$). Panels (*a–d*) correspond to the real part of modes M0, M1, M3 and M4. Here $R$ denotes the reattachment point.
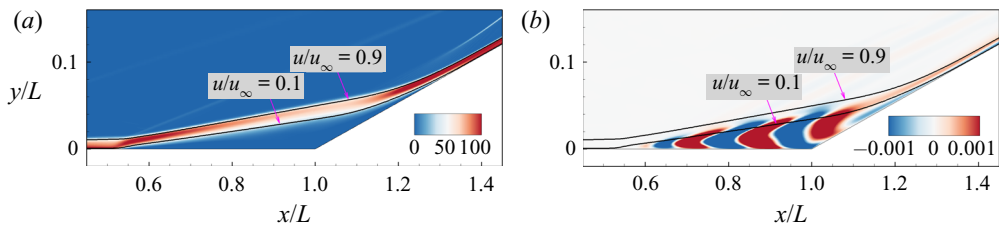


Figure 22. (*a*) Two isolines for $u/u_\infty = 0.1$ and $u/u_\infty = 0.9$ embedded in the contour of the velocity gradient $\partial u/\partial y$ which highlights the shear layer. (*b*) The same isolines as in panel (*a*) embedded in the contour showing the real part of mode M4.

figure 21(*a,b*) provides obvious evidence for the entrainment of the shear layer, where the spanwise velocity perturbation is persistently stretched downstream of reattachment. As aforementioned, the unsteadiness of the surface heat flux is featured by a propagation speed of $0.7u_\infty$. This speed is the convective speed at which the shear layer transports the unsteadiness downstream. Therefore, it is concluded that the intrinsic instability in the separation bubble is responsible for the unsteadiness of the considered compression ramp flow.

## 6. Concluding remarks

In the present work, a hypersonic compression ramp flow with a free stream Mach number of 7.7 and a free stream Reynolds number of $4.2 \times 10^5$ based on the flat plate length has been numerically investigated. The DNS results agree well with experimental data in terms of the time-averaged wall pressure and surface heat flux distributions as well as the wavelength of the observed heat flux streaks. Grid-convergence has been achieved for a mesh resolution of 124 million grid points regarding the flow phenomenon of interest.

It was shown that in the absence of external disturbances, streamwise heat flux streaks form on the ramp surface downstream of reattachment. The streaks are non-uniformly distributed in the spanwise direction, which is consistent with experimental observations (Simeonides & Haase 1995; Chuvakhov *et al.* 2017; Roghelia *et al.* 2017*a*,*b*). The DNS results indicate that the considered compression ramp flow initially undergoes an exponential growth stage and subsequently a stage of nonlinear saturation until the quasi-steady state is achieved. At the exponential growth stage, the flow behaviour is in good agreement with GSA predictions. Particularly, the mode shape, growth rate and spanwise wavelength of the three-dimensional perturbation are identical with those of the most unstable mode identified by GSA. The footprints of the global unstable modes are also observed in the saturated flow.

The saturated flow was shown to be unsteady. Downstream of reattachment, the surface heat flux exhibits a strong fluctuation associated with a broadband spectrum. The dominating frequencies are concentrated on the low-frequency region. Moreover, the fluctuation of the heat flux and therewith the unsteadiness of the heat flux streaks is coupled with a pulsation of the reattachment position. The downstream flow unsteadiness was shown to originate from the separation bubble flow.

Dynamic mode decomposition (standard DMD and SPDMD) was then employed to analyse the dominant oscillatory modes in the saturated separation bubble flow. The identified modes having strongest influence on the given snapshot sequence are also characterised by low frequencies similar to those found by the PSD analysis. These oscillatory modes exhibit streamwise periodicity in the separation bubble. This flow structure is linked to the downstream reattached flow by the shear layer above the separation bubble. The oscillatory modes extracted by DMD share similar flow structures with the oscillatory modes found by the present GSA as well as the low-frequency oscillatory mode found by Sidharth *et al.* (2018) for a separated double wedge flow. Therefore, it can be concluded that the unsteadiness of the considered hypersonic compression ramp flow has its origin in the intrinsic instabilities of the fluid dynamic system.

While centrifugal and baroclinic effects play an important role in amplifying external disturbances and generating streamwise streaks (Zapryagaev *et al.* 2013; Dwivedi *et al.* 2019), the present analyses demonstrate that in the absence of forced external disturbances, the spanwise interval between the surface heat flux streaks downstream of the separation region agrees well with the higher harmonics of the most unstable global modes. Therefore, the importance of instabilities in the separation bubble in the formation of downstream heat flux streaks, which has been extensively investigated by Sidharth *et al.* (2017, 2018) for different geometries, is confirmed. The three-dimensionality and unsteadiness triggered by the global instabilities of the dynamic system may destabilise the flow and cause transition to turbulence in a more complex manner, which deserves further investigation.

**Supplementary movie.** Supplementary movie is available at https://doi.org/10.1017/jfm.2020.1093.

**Author ORCIDs.**

🔾 Shibin Cao https://orcid.org/0000-0001-9579-0276;

🔾 Jiaao Hao https://orcid.org/0000-0002-8571-4728;

🔾 Chih-Yung Wen https://orcid.org/0000-0002-1181-8786.

REFERENCES

ANDERSON, J.D. JR. 2006 *Hypersonic and High-Temperature Gas Dynamics*. American Institute of Aeronautics and Astronautics.

BENAY, R., CHANETZ, B., MANGIN, B., VANDOMME, L. & PERRAUD, J. 2006 Shock wave/transitional boundary-layer interactions in hypersonic flow. *AIAA J.* **44** (6), 1243–1254.

CAO, S., KLIOUTCHNIKOV, I. & OLIVIER, H. 2019*a* Görtler vortices in hypersonic flow on compression ramps. *AIAA J.* **57** (9), 3874–3884.

CAO, S., KLIOUTCHNIKOV, I. & OLIVIER, H. 2019*b* Influence of the separation bubble flow at a compression ramp on Görtler-type vortices. In *Proceedings of the 32nd International Symposium on Shock Waves*, pp. 899–909. Research Publishing.

CAO, S., KLIOUTCHNIKOV, I. & OLIVIER, H. 2020 Görtler number evaluation for laminar separated hypersonic compression ramp flow. *AIAA J.* **58** (8), 3706–3710.

CHUVAKHOV, P.V., BOROVOY, V.Y., EGOROV, I.V., RADCHENKO, V.N., OLIVIER, H. & ROGHELIA, A. 2017 Effect of small bluntness on formation of Görtler vortices in a supersonic compression corner flow. *J. Appl. Mech. Tech. Phys.* **58** (6), 975–989.

CLEMENS, N.T. & NARAYANASWAMY, V. 2014 Low-frequency unsteadiness of shock wave/turbulent boundary layer interactions. *Annu. Rev. Fluid Mech.* **46**, 469–492.

DWIVEDI, A., SIDHARTH, G.S., NICHOLS, J.W., CANDLER, G.V. & JOVANOVIĆ, M.R. 2019 Reattachment streaks in hypersonic compression ramp flow: an input–output analysis. *J. Fluid Mech.* **880**, 113–135.

GAGEIK, M., KLIOUTCHNIKOV, I. & OLIVIER, H. 2015 Comprehensive mesh study for a direct numerical simulation of the transonic flow at $Re_c = 500\,000$ around a NACA 0012 airfoil. *Comput. Fluids* **122**, 153–164.

GINOUX, J.J. 1971 Streamwise vortices in reattaching high-speed flows – a suggested approach. *AIAA J.* **9** (4), 759–760.

HENDRICKSON, T.R., KARTHA, A. & CANDLER, G.V. 2018 An improved Ducros sensor for the simulation of compressible flows with shocks. *AIAA Paper* 2018-3710.

HERMES, V., KLIOUTCHNIKOV, I. & OLIVIER, H. 2012 Linear stability of WENO schemes coupled with explicit Runge–Kutta schemes. *Intl J. Numer. Meth. Fluids* **69** (6), 1065–1095.

HILDEBRAND, N., DWIVEDI, A., NICHOLS, J.W., JOVANOVIĆ, M.R. & CANDLER, G.V. 2018 Simulation and stability analysis of oblique shock-wave/boundary-layer interactions at Mach 5.92. *Phys. Rev. Fluids* **3** (1), 013906.

INGER, G.R. 1977 Three-dimensional heat-and mass-transfer effects across high-speed reattaching flows. *AIAA J.* **15** (3), 383–389.

JIANG, G. & SHU, C. 1996 Efficient implementation of weighted ENO schemes. *J. Comput. Phys.* **126** (1), 202–228.

JOVANOVIĆ, M.R., SCHMID, P.J. & NICHOLS, J.W. 2014 Sparsity-promoting dynamic mode decomposition. *Phys. Fluids* **26** (2), 024103.

KAVUN, I.N., LIPATOV, I.I. & ZAPRYAGAEV, V.I. 2019 Flow effects in the reattachment region of supersonic laminar separated flow. *Intl J. Heat Mass Transfer* **129**, 997–1009.

KLIOUTCHNIKOV, I., CAO, S. & OLIVIER, H. 2017 DNS of hypersonic ramp flow on a supercomputer. In *International Symposium on Shock Waves*, pp. 897–903. Springer.

LI, X.S., DEMMEL, J.W., GILBERT, J.R., GRIGORI, L., SHAO, M. & YAMAZAKI, I. 1999 *SuperLU Users' Guide*. Lawrence Berkeley National Laboratory.

DE LUCA, L., CARDONE, G., DE LA CHEVALERIE, D.A. & FONTENEAU, A. 1995 Viscous interaction phenomena in hypersonic wedge flow. *AIAA J.* **33** (12), 2293–2298.

MACCORMACK, R.W. 2014 *Numerical Computation of Compressible and Viscous Flow*. American Institute of Aeronautics and Astronautics.

Mani, A. 2012 Analysis and optimization of numerical sponge layers as a nonreflective boundary treatment. *J. Comput. Phys.* **231** (2), 704–716.

Matsumura, S., Schneider, S.P. & Berry, S.A. 2005 Streamwise vortex instability and transition on the Hyper-2000 scramjet forebody. *J. Spacecr. Rockets* **42** (1), 78–89.

Navarro-Martinez, S. & Tutty, O.R. 2005 Numerical simulation of Görtler vortices in hypersonic compression ramps. *Comput. Fluids* **34** (2), 225–247.

Ohmichi, Y. & Suzuki, K. 2013 Three-dimensional numerical simulation of Görtler vortices in hypersonic compression ramp. *AIAA Paper* 2013-262.

Pasquariello, V., Hickel, S. & Adams, N.A. 2017 Unsteady effects of strong shock-wave/boundary-layer interaction at high Reynolds number. *J. Fluid Mech.* **823**, 617–657.

Priebe, S. & Martín, M.P. 2012 Low-frequency unsteadiness in shock wave–turbulent boundary layer interaction. *J. Fluid Mech.* **699**, 1–49.

Robinet, J. 2007 Bifurcations in shock-wave/laminar-boundary-layer interaction: global instability approach. *J. Fluid Mech.* **579**, 85–112.

Roghelia, A., Chuvakhov, P.V., Olivier, H. & Egorov, I. 2017*a* Experimental investigation of Görtler vortices in hypersonic ramp flows behind sharp and blunt leading edges. *AIAA Paper* 2017-3463.

Roghelia, A., Olivier, H., Egorov, I. & Chuvakhov, P. 2017*b* Experimental investigation of Görtler vortices in hypersonic ramp flows. *Exp. Fluids* **58** (10), 139.

Schmid, P.J. 2010 Dynamic mode decomposition of numerical and experimental data. *J. Fluid Mech.* **656**, 5–28.

Sidharth, G.S., Dwivedi, A., Candler, G.V. & Nichols, J.W. 2017 Global linear stability analysis of high speed flows on compression ramps. *AIAA Paper* 2017-3455.

Sidharth, G.S., Dwivedi, A., Candler, G.V. & Nichols, J.W. 2018 Onset of three-dimensionality in supersonic flow over a slender double wedge. *Phys. Rev. Fluids* **3** (9), 093901.

Simeonides, G. & Haase, W. 1995 Experimental and computational investigations of hypersonic flow about compression ramps. *J. Fluid Mech.* **283**, 17–42.

Sorensen, D., Lehoucq, R., Yang, C. & Maschhoff, K. 1996–2008 ARPACK software.

Theofilis, V. 2011 Global linear instability. *Annu. Rev. Fluid Mech.* **43**, 319–352.

Theofilis, V., Hein, S. & Dallmann, U. 2000 On the origins of unsteadiness and three-dimensionality in a laminar separation bubble. *Phil. Trans. R. Soc. Lond.* A **358** (1777), 3229–3246.

Welch, P. 1967 The use of fast fourier transform for the estimation of power spectra: a method based on time averaging over short, modified periodograms. *IEEE Trans. Audio Electroacoust.* **15** (2), 70–73.

Yang, L., Zare-Behtash, H., Erdem, E. & Kontis, K. 2012 Investigation of the double ramp in hypersonic flow using luminescent measurement systems. *Exp. Therm. Fluid Sci.* **40**, 50–56.

Zapryagaev, V.I., Kavun, I.N. & Lipatov, I.I. 2013 Supersonic laminar separated flow structure at a ramp for a free-stream Mach number of 6. *Prog. Flight Phys.* **5**, 349–362.